Unifying theory of scaling in drop impact: Forces & maximum spreading diameter

Vatsal Sanjay[1,*] and Detlef Lohse[1,2,†]

[1] *Physics of Fluids Group, Max Planck Center Twente for Complex Fluid Dynamics, and J. M. Burgers Center for Fluid Dynamics, University of Twente, P.O. Box 217, 7500AE Enschede, Netherlands*

[2] *Max Planck Institute for Dynamics and Self-Organisation, Am Fassberg 17, 37077 Göttingen, Germany*

(Dated: August 22, 2024)

Abstract

The dynamics of drop impact on a rigid surface – omnipresent in nature and technology – strongly depends on the droplet's velocity, its size, and its material properties. The main characteristics are the droplet's force exerted on the surface and its maximal spreading radius. The crucial question is: How do they depend on the (dimensionless) control parameters, which are the Weber number We (non-dimensionalized kinetic energy) and the Ohnesorge number Oh (dimensionless viscosity)? Here we perform direct numerical simulations over the huge parameter range $1 \leq We \leq 10^3$ and $10^{-3} \leq Oh \leq 10^2$ and in particular develop a unifying theoretical approach, which is inspired by the Grossmann-Lohse theory for wall-bounded turbulence [J. Fluid Mech. 407, 27 (2000); PRL 86, 3316 (2001)]. The key idea is to split the energy dissipation rate into the different phases of the impact process, in which different physical mechanisms dominate. The theory can consistently and quantitatively account for the We and Oh dependences of the maximal impact force and the maximal spreading diameter over the huge parameter space. It also clarifies why viscous dissipation plays a significant role during impact, even for low-viscosity droplets (low Oh), in contrast to what had been assumed in prior theories.

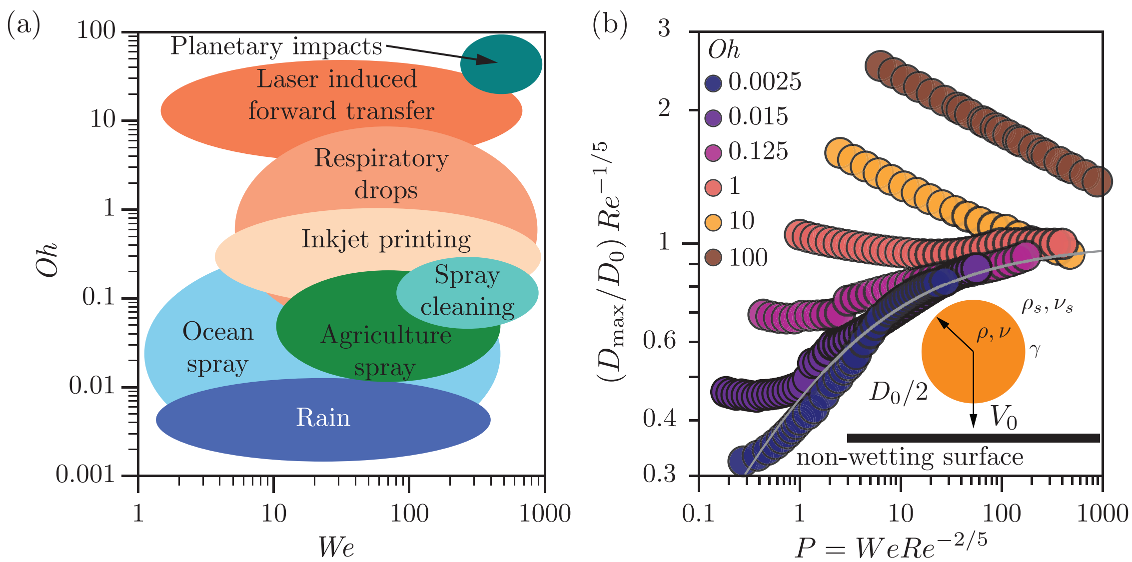

FIG. 1. (a) Typical values for We and Oh of drop impact events with relevance in nature and technology. (b) Maximal droplet spreading diameter (compensated by $Re^{1/5}$ for better visibility) vs the impact parameter $P = WeRe^{-2/5}$ from our numerical simulations, for various values of Oh (see legend). Also shown is the empirical fit proposed in ref. [10] (grey line), which does not work for large Oh and has limitations for small P.

Droplet impact on a rigid surface is omnipresent and very relevant in nature and technology [1–3]. Examples are rain [4], inkjet printing [5], spray coating [6], criminal forensics [7], and respiratory droplets [8], showing a plethora of different phenomena, depending on the droplet's velocity V_0, its diameter D_0, and its material properties (density ρ, dynamic viscosity μ, and surface tension γ). In dimensionless form, these control parameters are commonly (and for Newtonian droplets according to the Π-theorem completely) expressed as Weber number $We \equiv \rho V_0^2 D_0/\gamma$ and Ohnesorge number $Oh \equiv \mu/(\rho\gamma D_0)^{1/2}$; the Reynolds number then follows as $Re = \sqrt{We}/Oh$ and so does the so-called impact parameter as $P = WeRe^{-2/5}$. The huge range over which the control parameters of the above natural and industrial droplet impact events can occur – at least 5 orders of magnitude in We and 4 order of magnitude in Oh – are visualized in the $We - Oh$ parameter space of figure 1a. Gravity normally does not play any or hardly any role in these impact processes and in this paper it is assumed to be zero. We moreover assume an axisymmetrical impact; for discussions on splashing, which sets in for very large impact velocities and at later times during the impact event, we refer to [9].

At impact, the drop encounters a normal reaction force [11–13], which transforms its vertical momentum into radial spreading [9]. During this spreading phase, inertia drives the droplet outwards until it reaches its maximum diameter $D_{\max}$ [14], where surface tension and viscosity collectively limit further deformation [15]. What is of particular relevance for applications are this maximal spreading diameter $D_{\max}$ and the maximal normal force $F_{\max}$ which the drop exerts on the surface at impact. For the former, traditionally, scaling relations were sought for, such as $D_{\max}/D_0 \sim Re^{1/3}$ [16] or $\sim Re^{1/5}$ [17, 18] for viscous drop impact, $D_{\max}/D_0 \sim We^{1/4}$ for larger impact velocities [19], or $D_{\max}/D_0 \sim We^{1/2}$ for very large impact velocities [20–23]. However, it is clear that none of these scaling relations can hold in the *whole* parameter space of figure 1a. Even empirically modelled transitions between two different scaling laws fail, as shown in figure 1b, where we compare our numerical simulations (as detailed below) with the popular empirically modelled smooth transition between two limiting scaling relations [10]

$$\frac{D_{\max}}{D_0} = a_0 \frac{Re^{1/5} P^{1/2}}{a_1 + P^{1/2}}. \tag{1}$$

Here $a_0 = 1$ and $a_1 = 1.24 \pm 0.01$ are empirical constants obtained from fitting experimental data [10]. While eq. (1) reasonably well describes the data for droplets with small viscosities (small Oh) and large impact velocities (large P), it does so less for small P, and not at all for large Oh (cf. fig. 1b).

The objective of this Letter is to achieve a unifying physical understanding of how the maximal spreading diameter $D_{\max}$ and the maximal normal force $F_{\max}$ [25] dependent on the system's control parameters We and Oh, for the whole huge relevant parameter space of fig. 1. To do so, we first perform over 16000 direct numerical simulations (with the volume-of-fluid solver Basilisk [26, 27], detailed in the SI) of the drop impact process over this whole $We - Oh$ parameter space, see fig. 2a, and numerically obtain the dependencies $F_{\max}(We, Oh)$ and $D_{\max}(We, Oh)$, see figures 3 and 4. We then, in the main part of this Letter, develop a unifying theory to account for these dependencies. It is inspired by Grossmann's and Lohse's unifying theory ("GL-theory") for thermally driven turbulence [28–31], whose key idea it is to spatially decompose the energy dissipation rate into boundary layer and bulk contributions and to model these individually, based on the different flow physics in the boundary layer and in the bulk. The GL-theory gives the full dependencies of the response parameters (in that case the overall heat transfer and turbulence intensity)

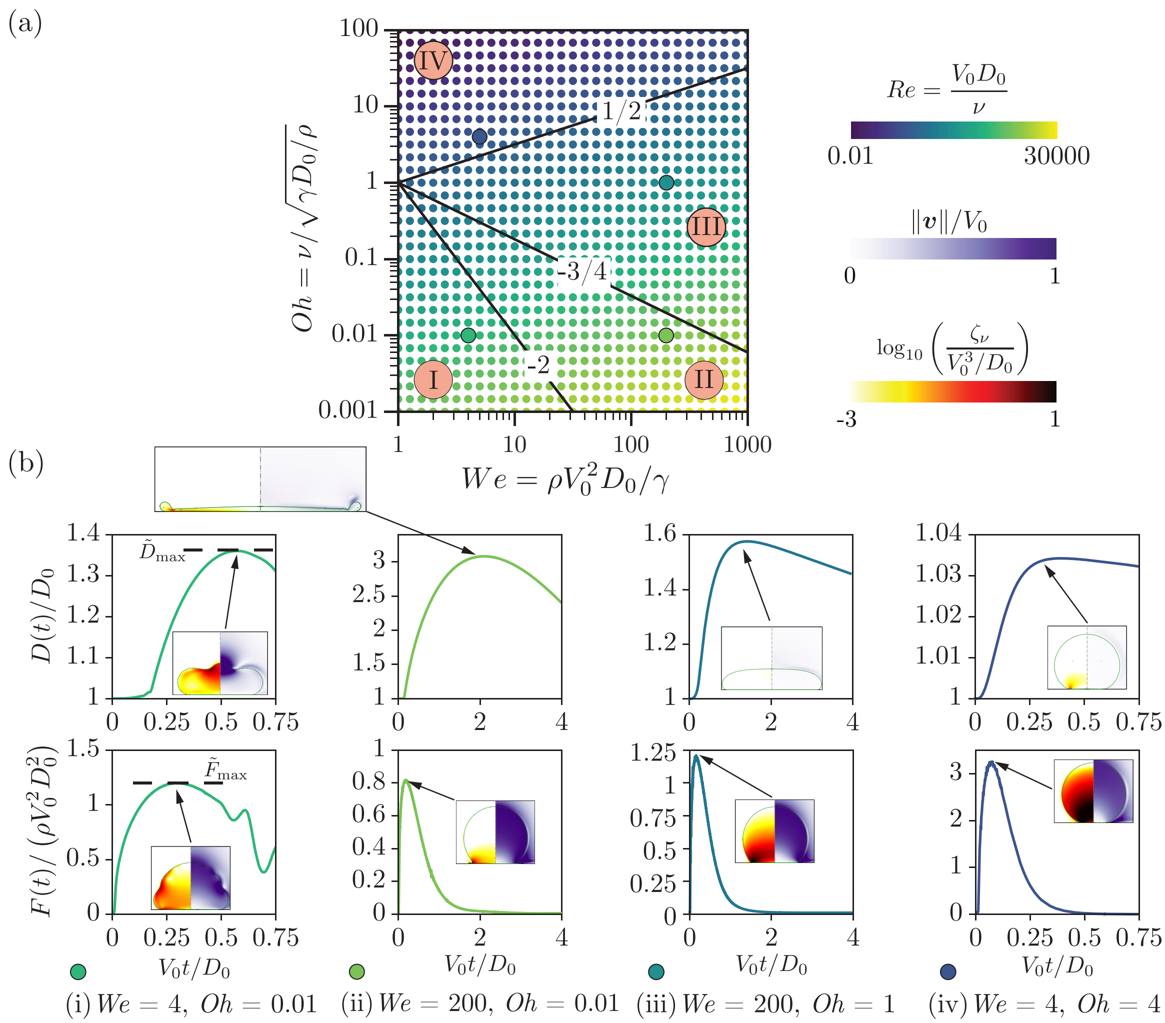

FIG. 2. (a) Phase space in the Oh-We plane, illustrating the range of simulations conducted in this work, with simulation points (for clarity, only every 16$^{\text{th}}$ case is shown) colored according to the Reynolds number $Re = \sqrt{We}/Oh$. The three black lines (with slopes -2, $-3/4$, and $1/2$, respectively) delineate the four different regimes of the drop spreading process (see table in fig. 5): Regime I: unbounded dissipation (small Oh and small We); Regime II: vertically bounded dissipation (small Oh and large We); Regime III: fully bounded dissipation (medium Oh and large We); Regime IV: no spreading phase (large Oh). (b) Four typical cases across the phase space, representing each of the four regimes. The plots show the spreading diameter $D(t)$ and the normal reaction force $F(t)$. We chose (We, Oh) = (i) $(4, 4)$, (ii) $(4, 0.01)$, (iii) $(200, 1)$, and (iv) $(200, 0.01)$. For each case, the insets show the drop at the moments of maximum impact force and later at maximum spreading diameter. The left part of each numerical snapshot depicts the dimensionless local viscous dissipation rates $\zeta_\nu(\boldsymbol{x}, t)$ [24] on a $\log_{10}$ scale, and the right part shows the local velocity field magnitude normalized by the impact velocity.

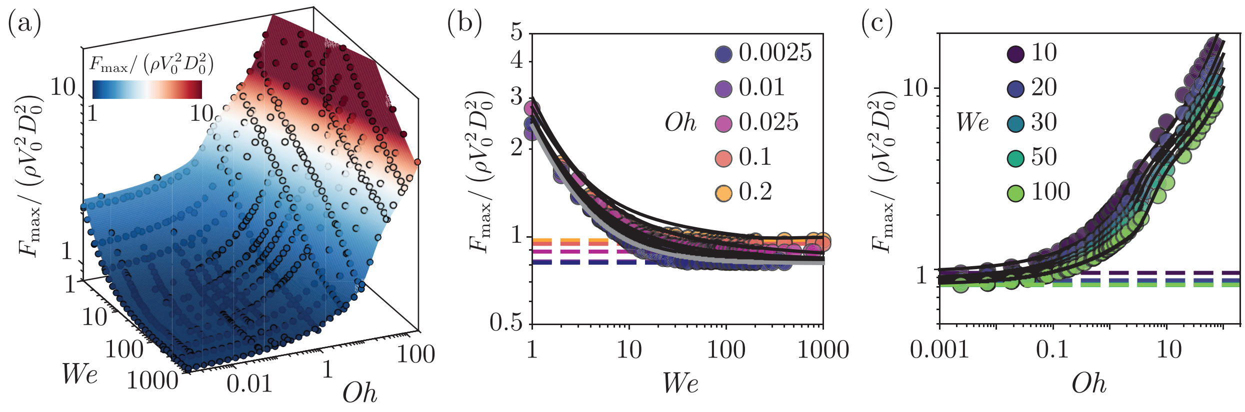

FIG. 3. Maximum impact force $F_{\max}$ compensated with the inertial force scale $\rho V_0^2 D_0^2$ as a function of (a) Oh and We in a 3D plot, (b) We at different Oh and (c) Oh at different We. The data points represent the simulation results, while the surface in (a) and the lines in (b)–(c) depict the results of the proposed theoretical model. The grey solid line in (b) represents the solution ignoring viscous dissipation. The dashed lines in (b) and (c) mark the asymptotes $We \gg 1$ and $Oh \ll 1$, respectively.

on the control parameters. Here, for the droplet impact problem, the decomposition of the energy dissipation rate will not be spatially, but temporally, namely splitting it into the impact phase and the spreading phase, each characterized by different scaling laws. This temporal decomposition allows us to disentangle the respective influences of these two phases on the maximal force and the maximal spreading diameter, and to come to a unifying physical understanding of the dependencies $F_{\max}\left(We, Oh\right)$ and $D_{\max}\left(We, Oh\right)$ over the whole huge control parameter space, consistent with our numerical results, cf. figures 3 and 4.

Energy balance to obtain D_{max}: We start by formulating the exact energy balance for the drop impact process [23, 32],

$$K_{\mathrm{cm}}(t=0) = K_{\mathrm{cm}}(t) + K_{\mathrm{int}}(t) + S(t) + mE_d(t), \tag{2}$$

where $K_{\mathrm{cm}}(t=0) = mV_0^2/2$ is the center of mass kinetic energy at the moment of impact (fig. 2a), which is the total energy of the system with mass m. Upon impact and spreading, part of this initial kinetic energy remains as the center of mass kinetic energy $K_{\mathrm{cm}}(t)$. Another part transforms into internal kinetic energy $K_{\mathrm{int}}(t)$ due to the redirection of vertical momentum into radial spreading. The third term on the rhs is the gain $S(t)$ of surface energy

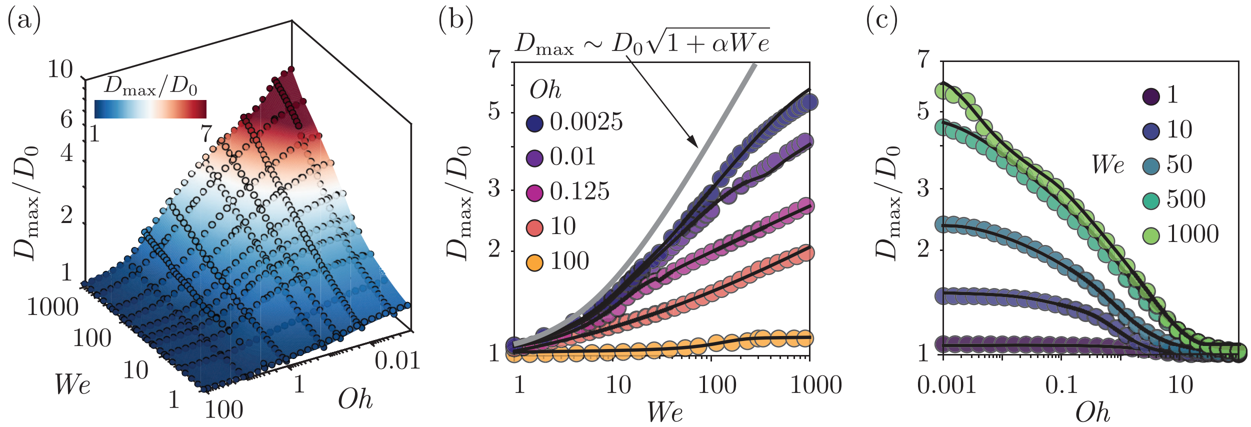

FIG. 4. Maximum spreading diameter $D_{\max}$ normalized by the initial drop diameter D_0 as a function of (a) Oh and We in a 3D plot, (b) We for various Oh, and (c) Oh for different We. The data points represent the simulation results, while the surface in (a) and the lines in (b)–(c) depict the results of the proposed theoretical model. The gray solid line in (b) represents the solution ignoring viscous dissipation.

through the spreading process, as compared to the drop's surface energy at $t = 0$, when it is minimal, because the drop then is spherical. Finally, the last term $mE_d(t)$ accounts for the total viscous dissipation, which reduces the available energy over time, where $E_d(t)$ is the viscous dissipation per unit mass up to time t. It is obtained from time-integration of the energy dissipation rate per mass and time $\varepsilon(t)$ as $E_d(t) = \int_0^t \varepsilon(t)dt$.

When is the maximal spreading $D_{\max}$ achieved? Scaling-wise, this spreading time τ_s is obtained from balancing inertia and capillarity, $\tau_s \sim \sqrt{\rho D_0^3/\gamma}$, also reflecting the known analogy between the first phase of drop spreading and the oscillation of a free droplet [33–35]. The surface energy at that moment $t = \tau_s$ of maximal spreading is directly related to the maximum spreading diameter $D_{\max}$ as $S(t = \tau_s) \sim \gamma\,(D_{\max}^2 - D_0^2)$. Moreover, at that moment, the drop's center-of-mass kinetic energy and its internal kinetic energy are both zero, $K_{\rm cm}(\tau_s) = K_{\rm int}(\tau_s) = 0$, as illustrated in the insets of fig. 2(b) [35, 36]. Then the maximum spreading diameter simply results from balancing the initial kinetic energy with the surface energy increment and the total viscous dissipation during spreading ($0 \le t \le \tau_s$),

$$K_{\rm cm}(t = 0) = S(t = \tau_s) + mE_d(t = \tau_s). \tag{3}$$

We can rewrite eq. (3) as

$$D_{\max} = D_0 \sqrt{\left(\alpha_0 + \alpha_1 We \left(1 - \frac{E_d(t = \tau_s)}{V_0^2}\right)\right)}. \tag{4}$$

Here we have replaced the scaling relations with exact equalities, which introduces the free parameters α_i, $i = 0, 1$.

Force balance to obtain F_{max}: To obtain the force balance, we differentiate the energy transfer rates in eq. (2) with respect to time. The derivative $\dot{K}_{\mathrm{cm}}(t) = -F(t)V_{\mathrm{cm}}(t)$ straightforwardly gives the normal reaction force $F(t)$, where $V_{\mathrm{cm}}(t)$ is the center of mass velocity. We obtain the maximal normal force $F_{\max} \approx F(t = \tau_\rho)$ from using this force balance at the inertial time scale $t = \tau_\rho \equiv D_0/V_0$,

$$F_{\max} = \frac{1}{V_0}\left(\dot{K}_{\mathrm{int}}(t = \tau_\rho) + \dot{S}(t = \tau_\rho) + m\varepsilon(t = \tau_\rho)\right). \tag{5}$$

At this time $t = \tau_\rho$, the drop only deforms locally at the south pole, which contacts the substrate, while the north pole is still descending with velocity V_0 [9, 21]. We emphasize that the maximum force occurs at $t = \tau_\rho$, much earlier than the maximum spreading at $t = \tau_s \gg \tau_\rho$ (fig. 2b).

Next, we evaluate the internal kinetic energy of the spreading drop as $K_{\mathrm{int}}(t) \sim mV_{\mathrm{f}}^2/2$, where V_{f} is the velocity at which the contact footprint D_{f} grows on the rigid surface. Intriguingly, both the inertial [37, 38] and viscous [39–42] regimes exhibit the same scaling behavior: $D_{\mathrm{f}} \sim \sqrt{V_0 D_0 t}$. Consequently, $\dot{K}_{\mathrm{int}}(t) \sim mV_0D_0/t^2$, see refs. [24, 43] for a detailed discussion. To calculate the rate of surface energy change, we assume that the drop behaves like a deformable cylinder of constant volume. Thus, the scales for the time derivative of internal energy and surface energy at the inertial time scale are given by

$$\dot{K}_{\mathrm{int}}^* \equiv \dot{K}_{\mathrm{int}}(t \approx \tau_\rho) \sim \rho V_0^3 D_0^2, \text{ and} \tag{6}$$

$$\dot{S}^* \equiv \dot{S}(t \approx \tau_\rho) \sim \gamma D_0 V_0, \tag{7}$$

respectively. We can then insert the energy and energy rate scales calculated above to simplify eq. (5) to

$$F_{\max} = \rho V_0^2 D_0^2 \left(\beta_0 + \frac{\beta_1}{We} + \frac{\varepsilon(t = \tau_\rho)}{V_0^3/D_0}\right). \tag{8}$$

Again we have replaced the scaling relations with exact equalities, which introduces the free parameters β_i, $i = 0, 1$.

Inertial limits $Oh \to 0$: Before we calculate the total viscous dissipation $E_d(t)$ at time $t = \tau_s$ in eq. (4) and the viscous dissipation rate $\varepsilon(t) = \dot{E}_d(t)$ at time $t = \tau_\rho$ in eq. (8) in order to obtain $F_{\max}(We, Oh)$ and $D_{\max}(We, Oh)$ for general We and Oh, we first discuss the inertial limits $Oh \to 0$ of eqs. (8) and (4). The resulting expression $F_{\max} = \rho V_0^2 D_0^2 (\beta_0 + \beta_1/We)$ in this limit is identical to the empirically relationship already proposed in ref. [9], which models the crossover from inertial dominance (first term) to capillary dominance (second term) with increasing We. This expression nicely approximates the impact force over two orders of magnitude in the Ohnesorge number $0.0025 < Oh < 0.2$, as shown in fig.3 and [15]. However, as expected, the agreement breaks down for moderate to large Oh (fig.3(c)), reflecting the relevance of the viscous contribution. Similarly, the inertial limit of eq. (4) gives $D_{\max}/D_0 \sim \sqrt{1 + \alpha We}$, which is shown in figure 4b as grey line and clearly does not describe the data for large Oh.

Key idea to calculate the energy dissipation rates for general (Oh, We): So it has become clear that for the general case it is crucial to calculate the energy dissipation rates in eqs. (4) and (8). To do so, we got inspired by the GL-theory [28–30, 44] for wall-bounded turbulent thermal convection. The key idea of that theory is to spatially split the viscous dissipation rate into boundary layer and bulk contributions and estimate those separately, reflecting the different flow physics in these two regions. Instead of the spatial decomposition employed in that theory, here, we *temporally* decompose the viscous dissipation rate, by dividing the whole drop impact process into an impact phase (index "i") and a spreading phase (index "s").

Maximum impact force for general We and Oh: For the general case of eq. (8), we have to evaluate the energy dissipation rate $\varepsilon^* \equiv \varepsilon(t \approx \tau_\rho)$. During the impact phase, which takes place on the inertial time scale τ_ρ, the drop's south pole halts [45, 46], creating a velocity gradient near the surface across a boundary layer with thickness $\lambda_i(t)$, observable in the black region of fig. 2(b). This gradient $V_0/\lambda_i(t)$ propagates to the north pole, building up a viscous velocity gradient in the drop. The thickness of this boundary layer during the impact phase scales as $\lambda_i(t) \sim \sqrt{\nu t}$, according to the Prandtl-Blasius boundary layer theory [47–49]. Here $\nu = \mu/\rho$ is the kinematic viscosity. In this phase the viscous dissipation rate $\varepsilon_{i,\mathrm{PB}}(t)$ within the volume $\Omega_{\nu,i}(t) \sim D_\mathrm{f}(t)^2 \lambda_i(t)$ is approximated as

$$\varepsilon_{i,\mathrm{PB}}(t) \sim \frac{\nu}{D_0^3} \left(\frac{V_0}{\lambda_i(t)} \right)^2 D_\mathrm{f}(t)^2 \lambda_i(t) \sim \sqrt{\frac{\nu t}{D_0^2}} \frac{V_0^3}{D_0}. \tag{9}$$

For very viscous liquids (large ν and thus large Oh) the boundary layer thickness $\lambda_i \sim \sqrt{\nu t}$ very quickly reaches the full diameter D_0 of the droplet and then obviously no longer increases, $\lambda_i \sim D_0$, as illustrated in the last line of the table in figure 5. Then the energy dissipation rate $\varepsilon_{i,\mathrm{PB}}(t)$ of eq. (9), which holds during the Prandtl-Blasius phase of the impact phase, must be replaced by

$$\varepsilon_{i,\infty}(t) \sim \frac{\nu}{D_0^3}\left(\frac{V_0}{D_0}\right)^2 D_{\mathrm{f}}(t)^2 D_0 \sim \left(\frac{\nu t}{D_0^2}\right)\frac{V_0^3}{D_0}. \tag{10}$$

Here we chose the index "∞" in analogy to the notation of the GL-theory for thermally driven convection, where the corresponding regime, in which the boundary layer reaches the system size, is also noted with that index. This extra subphase of the impacting phase can only occur when the viscous timescale $\tau_\nu \equiv D_0^2/\nu$ is faster than the impact timescale τ_ρ, i.e., when $\tau_\nu \ll \tau_\rho$, or, in other words, when the drop impact Reynolds number $Re \equiv V_0 D_0/\nu \ll 1$, i.e., indeed only in the viscous case. Then, to estimate the mean dissipation at time $t \approx \tau_\rho$, we must consider the two subphases of the impacting phase separately.

So, in summary, the estimate for the dissipation rate at the time $t \approx \tau_\rho$ of the maximal force $F_{\max}$ is

$$\varepsilon^* \equiv \varepsilon(t \approx \tau_\rho) \sim \begin{cases} \overbrace{\frac{d}{dt}\left(\int_0^{\tau_\rho} \varepsilon_{i,\mathrm{PB}}(t)dt\right)}^{\varepsilon_{i,\mathrm{PB}}(t\approx\tau_\rho)} & \text{for } Re > 1\text{, and} \\ \underbrace{\frac{d}{dt}\left(\int_0^{\tau_\nu} \varepsilon_{i,\mathrm{PB}}(t)dt\right)}_{\varepsilon_{i,\mathrm{PB}}(t\approx\tau_\nu)} + \underbrace{\frac{d}{dt}\left(\int_{\tau_\nu}^{\tau_\rho} \varepsilon_{i,\infty}(t)dt\right)}_{\varepsilon_{i,\infty}(t\approx\tau_\rho)-\varepsilon_{i,\infty}(t\approx\tau_\nu)} & \text{for } Re < 1 \end{cases} \tag{11}$$

which, when filled into eq. (8), gives our final result for the (nondimensionalized) maximal impact force,

$$\frac{F_{\max}}{\rho V_0^2 D_0^2} = \beta_0 + \frac{\beta_1}{We} + \begin{cases} k_0\left(Oh/\sqrt{We}\right)^{1/2} & \text{for } Re > 1 \\ m_0 + m_1\left(Oh/\sqrt{We} - 1\right) & \text{for } Re < 1 \end{cases} \tag{12}$$

Here, again, the scaling relations have been replaced by an equal sign and the corresponding prefactors (here k_0, m_0, m_1) that must be fitted to trustable data (see SI for details), in perfect analogy to what had to be done in the GL-theory for thermal convection. The result is shown in fig. 3 and compared to the numerical data, which are excellently described.

Maximum spreading diameter for general We and Oh: As seen above, the viscous contribution $E_d(t = \tau_s) = \int_0^{\tau_s} \varepsilon(t)dt$ in eq. (4) is highly relevant to obtain the general case for

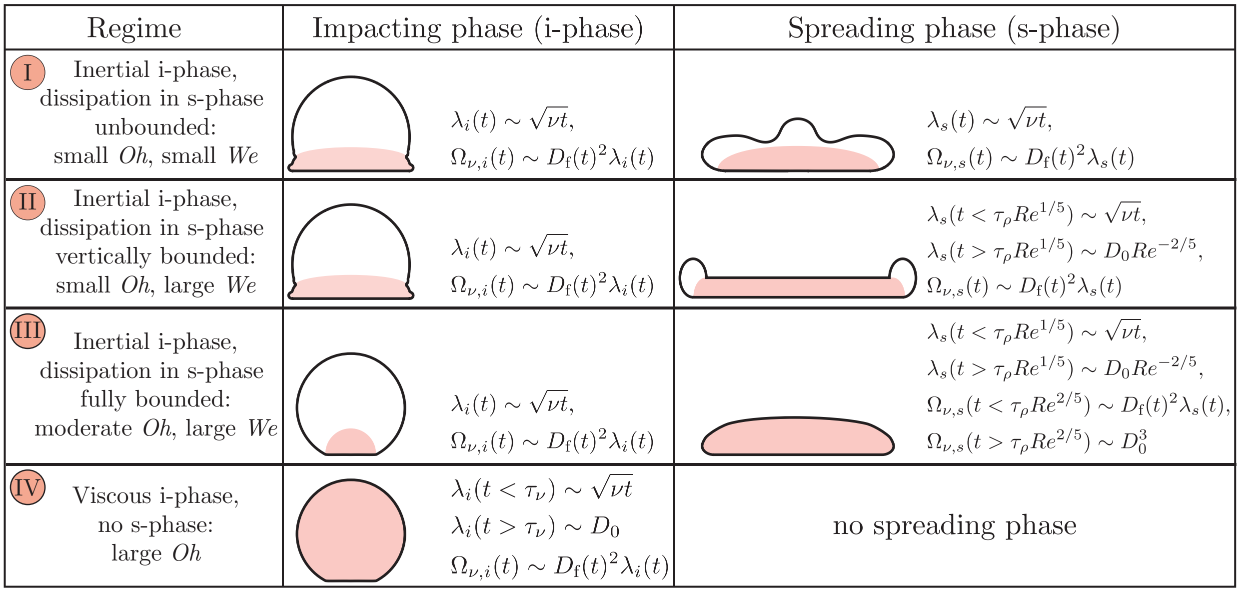

FIG. 5. Sketches of the impacting phase (i-phase) and the spreading phase (s-phase) with the respective scaling relations for the four regimes I, II, III, and IV.

the maximal spreading diameter $D_{\rm max}$. To calculate it, as explained above, we have to take notice of the different fluid dynamics in the impacting phase and in the spreading phase. We correspondingly decompose the total energy dissipation into

$$E_d(t = \tau_s) = \int_0^{\tau_\rho} \varepsilon_i(t) dt + \int_{\tau_\rho}^{\tau_s} \varepsilon_s(t) dt, \tag{13}$$

where

$$\varepsilon_i(t) \sim \frac{\nu}{D_0^3} \left(\frac{V_0}{\lambda_i(t)} \right)^2 \Omega_{\nu,i}(t) \quad \text{and} \tag{14}$$

$$\varepsilon_s(t) \sim \frac{\nu}{D_0^3} \left(\frac{V_{\rm f}(t)}{\lambda_s(t)} \right)^2 \Omega_{\nu,s}(t) \tag{15}$$

are the viscous dissipation rates in the impact and spreading time intervals, respectively.

The impact interval can be computed identically to what we have done already in equations (9) and (10) for the force calculation. What occurs in the spreading phase depends on Oh and We and can be classified into four different regimes, see fig. 2a and the right column in the table in figure 5:

I Regime I (small Oh and small We): The viscous boundary layer remains engulfed inside the falling drop and never reaches the north pole during impact or spreading. In this regime, the viscous boundary layer $\lambda_s(t)$ develops due to the radial spreading of the drop's foot $D_\mathrm{f}(t)$ on the rigid surface and follows the conventional Prandtl-Blasius scaling [47–49]. The volume $\Omega_{\nu,s}(t)$ where the dissipation occurs can be modeled as a cylinder with diameter $D_\mathrm{f}(t)$ and height $\lambda_s(t)$.

II Regime II (small Oh and large We): The viscous boundary layer stays inside the deforming drop during the impact but reaches the north pole in the spreading phase, with the dissipation region confined within the drop.

III Regime III (medium Oh and large We): Similar to Regime II, but the dissipation region spreads throughout the drop during the spreading phase.

IV Regime IV (large Oh): The viscous boundary layer reaches the north pole during impact, causing dissipation throughout the drop. This regime is identical to the ∞-regime encountered while evaluating the viscous dissipation rate in eq. (10).

We refer the readers to the supplementary material [24] for detailed calculations of the scaling behaviors in these four regimes and summarize them in the table in figure 5.

The transitions between these four regimes are characterized by the different physical balances resulting in specific scaling relationships (fig. 2). The transition from Regime I to II occurs when the viscous boundary layer reaches the north pole during spreading. To determine the crossover time to this regime, we use the trajectory of the drop's north pole, given by $D_0^3/(V_0^2t^2)$, independent of We and Oh for inertial impacts [21], and equate it to the growing boundary layer thickness $\lambda_s(t) \sim \sqrt{\nu t}$. Beyond this crossover, $\lambda_s(t)$ becomes time-invariant and equal to $D_0 Re^{-2/5}$ [21]. Consequently, the transition from regime I to II occurs at $\tau_s \sim \tau_\rho Re^{1/5}$, corresponding to $Oh \sim We^{-2}$. The transition from Regime II to III is marked by the dissipation region extending throughout the drop during spreading, occurring when $\Omega_{\nu,s}(t) \approx D_0^3$, giving $\tau_s \sim \tau_\rho Re^{2/5}$, corresponding to $Oh \sim We^{-3/4}$. Notably, once the dissipation has taken over the entire drop's volume, the drop's foot also becomes immobile, and the spreading phase ceases at $\tau_s \sim \tau_\rho Re^{2/5}$. Finally, the transition from Regime III to IV takes place when the viscous boundary layer reaches the north pole during impact, corresponding to $\tau_\rho \sim \tau_\nu$, $Re \sim 1$, or $Oh \sim \sqrt{We}$, as already explained above.

The next step is to plug in the relevant timescales in eq. (13) and to evaluate the integrals with the estimates (14) and (15). We obtain

$$\frac{E_d(t=\tau_s)}{V_0^2} \sim \begin{cases} \left(a_0 + a_1 We^{1/4}\right)/\sqrt{Re} & \text{in Regime I,} \\ \left(b_0 + b_1 Re^{1/10} + b_2 Re^{-1/10}\sqrt{We}\right)/\sqrt{Re} & \text{in Regime II,} \\ \left(c_0 + c_1 Re^{1/10} + c_2 Re^{3/10}\right)/\sqrt{Re} & \text{in Regime III,} \\ d_0 + d_1 Re + d_1/Re & \text{in Regime IV,} \end{cases} \tag{16}$$

which is then plugged into eq. (4) to get the final results for $D_{\max}(We, Oh)$. Again, in eq. (16), the scaling relations have been replaced by prefactors that must be fitted to trustable data of $D_{\max}(We, Oh)$, cf. SI. The result is shown in fig. 4 and compared to the numerical data, which again are excellently described.

We emphasize that, remarkably, even in the low-viscosity limit $Oh \to 0$ the viscous contribution (16) to the final result for $D_{\max}$ (cf. eq. (4)) cannot be neglected and does contribute! This for examples holds for water-like systems (which have $Oh \ll 1$), as we had already realized in ref. [32]. This dissipation occurs at impact, as depicted in the insets of fig. 2. Even for $Oh \to 0^+$, this dissipation remains substantial. We note that this also holds for the normal impact force (for $Re < 1$), see eq. (11). Such a singular limit is akin to the dissipative anomaly observed in fully developed turbulence [50–53], and we have been recently investigated similar singular limits also in the context of sheet retraction [54], sliding drops [55], converging gravito-capillary waves [56].

Conclusions and outlook: This study presents a comprehensive theoretical framework to elucidate the scaling laws governing the maximum impact force $F_{\max}(We, Oh)$ and the maximal spreading diameter $D_{\max}(We, Oh)$ of droplets upon impact. Inspired by the GL-theory for thermally driven turbulence, we systematically consider viscous dissipation rates across various regimes and allows for predictions. Our model covers five decades in the Ohnesorge number Oh and three decades in the Weber number We, effectively mapping the transitions between the different regimes. Future research could extend the present model in order to incorporate the effects of gravity, which influences the spreading diameter at moderate to high Oh numbers.

Our results illustrate that viscous dissipation significantly affects the maximum impact force and spreading diameter, even in regimes typically considered inertial, i.e., when Oh is small. For instance, the solid gray line in Fig. 4(b) represents the theoretical upper bound of the spreading diameter when viscous dissipation is neglected and totally fails to describe the data. Drop impact thus is an example for a singular limit in hydrodynamics. It underscores the importance of accounting for viscous effects in hydrodynamics systems in general, even in low-viscosity systems, reflecting the persistent contribution of dissipation even for $Oh \to 0^+$.

Our results also demonstrate the capacity of the key idea of the GL-theory, namely to decompose the energy dissipation rate of a hydrodynamic systems, either locally as in the original GL-theory [28, 29], or here temporally, and suggests to try such an approach also to other hydrodynamic problems.

Acknowledgements: The authors are grateful to Pierre Chantelot, Andrea Prosperetti, Uddalok Sen, and Vincent Bertin for the stimulating discussions, and to Anjali Suman for help with the implementation of the regression algorithm to find the prefactors in eqs. (12) and (16) [24]. We also acknowledge financial support from NWO and from Canon. The numerical simulations were carried out on the national e-infrastructure of SURFsara, a subsidiary of SURF cooperation, the collaborative ICT organization for Dutch education and research.

* vatsalsanjay@gmail.com

† d.lohse@utwente.nl

[1] C. Josserand and S. T. Thoroddsen, *Drop impact on a solid surface*, Annu. Rev. Fluid Mech. **48**, 365 (2016).

[2] A. L. Yarin, *Drop impact dynamics: Splashing, Spreading, Receding, Bouncing...*, Annu. Rev. Fluid Mech. **38**, 159 (2006).

[3] A. L. Yarin, I. V. Roisman, and C. Tropea, *Collision Phenomena in Liquids and Solids* (Cambridge University Press, Cambridge, 2017).

[4] A. M. Worthington, *XXVIII. On the forms assumed by drops of liquids falling vertically on a horizontal plate*, Proc. R. Soc. London, Ser. A **25**, 261 (1876).

[5] D. Lohse, *Fundamental fluid dynamics challenges in inkjet printing*, Annu. Rev. Fluid Mech. **54**, 349 (2022).

[6] J. Kim, *Spray cooling heat transfer: The state of the art*, Int. J. Heat Fluid Flow **28**, 753 (2007).

[7] F. R. Smith, C. Nicloux, and D. Brutin, *Influence of the impact energy on the pattern of blood drip stains*, Phys. Rev. Fluids **3**, 013601 (2018).

[8] L. Bourouiba, *The Fluid Dynamics of Disease Transmission*, Annu. Rev. Fluid Mech. **53**, 473 (2021).

[9] B. Zhang, V. Sanjay, S. Shi, Y. Zhao, C. Lv, and D. Lohse, *Impact forces of water drops falling on superhydrophobic surfaces*, Phys. Rev. Lett. **129**, 104501 (2022).

[10] N. Laan, K. G. de Bruin, D. Bartolo, C. Josserand, and D. Bonn, *Maximum diameter of impacting liquid droplets*, Phys. Rev. Appl. **2**, 044018 (2014).

[11] M. A. Nearing, J. M. Bradford, and R. D. Holtz, *Measurement of force vs. time relations for waterdrop impact*, Soil Sci. Soc. Am. J. **50**, 1532 (1986).

[12] B. R. Mitchell, J. C. Klewicki, Y. P. Korkolis, and B. L. Kinsey, *The transient force profile of low-speed droplet impact: measurements and model*, J. Fluid Mech. **867**, 300 (2019).

[13] X. Cheng, T.-P. Sun, and L. Gordillo, *Drop Impact Dynamics: Impact Force and Stress Distributions*, Annu. Rev. Fluid Mech. **54**, 57 (2021).

[14] S. Chandra and C. T. Avedisian, *On the collision of a droplet with a solid surface*, Proc. R. Soc. Lond. A **432**, 13 (1991).

[15] V. Sanjay, B. Zhang, C. Lv, and D. Lohse, *The role of viscosity on drop impact forces*, arXiv preprint (2024).

[16] L. Jørgensen, *Deformation of drops at low Reynolds number impact*, Phys. Rev. Fluids **9**, 083601 (2024).

[17] J. Madejski, *Solidification of droplets on a cold surface*, Int. J. Heat Mass Transfer **19**, 1009 (1976).

[18] A. I. Fedorchenko, A. B. Wang, and Y. H. Wang, *Effect of capillary and viscous forces on spreading of a liquid drop impinging on a solid surface*, Phys. Fluids **17**, (2005).

[19] C. Clanet, C. Béguin, D. Richard, and D. Quéré, *Maximal deformation of an impacting drop*, J. Fluid Mech. **517**, 199 (2004).

[20] T. Bennett and D. Poulikakos, *Splat-quench solidification: estimating the maximum spreading of a droplet impacting a solid surface*, J. Mater. Sci. **28**, 963 (1993).

[21] J. Eggers, M. A. Fontelos, C. Josserand, and S. Zaleski, *Drop dynamics after impact on a solid wall: Theory and simulations*, Phys. Fluids **22**, 062101 (2010).

[22] E. Villermaux and B. Bossa, *Drop fragmentation on impact*, J. Fluid Mech. **668**, 412 (2011).

[23] S. Wildeman, C. W. Visser, C. Sun, and D. Lohse, *On the spreading of impacting drops*, J. Fluid Mech. **805**, 636 (2016).

[24] See Supplemental Material at (URL to be inserted by the publisher) for a description of numerical methods, details of the various regimes and transition., 2024.

[25] We note that in singular cases the first impact peak need not be the largest: As our recent studies [9, 15] have indicated, under very specific conditions ($Oh \sim \mathcal{O}(10^{-3})$, $We \approx 9$), a second impact peak – after droplet recoil and connected to the bouncing up of the droplet – can exceed the first one due to a hydrodynamic singularity. For our considerations here it is not relevant.

[26] S. Popinet and collaborators, Basilisk C: Volume of Fluid method, http://basilisk.fr, 2013–now.

[27] V. Sanjay, Code repository: Impact forces of water drops falling on superhydrophobic surfaces, https://doi.org/10.5281/zenodo.7598181, 2023.

[28] S. Grossmann and D. Lohse, *Scaling in thermal convection: a unifying theory*, J. Fluid Mech. **407**, 27 (2000).

[29] S. Grossmann and D. Lohse, *Thermal convection for large Prandtl numbers*, Phys. Rev. Lett. **86**, 3316 (2001).

[30] D. Lohse and O. Shishkina, *Ultimate turbulent thermal convection*, Phys. Today **76**, 26 (2023).

[31] D. Lohse and O. Shishkina, *Ultimate Rayleigh–Bénard turbulence*, Rev. Mod. Phys. **96**, 035001 (2024).

[32] V. Sanjay, P. Chantelot, and D. Lohse, *When does an impacting drop stop bouncing?*, J. Fluid Mech. **958**, A26 (2023).

[33] D. Richard, C. Clanet, and D. Quéré, *Contact time of a bouncing drop*, Nature **417**, 811 (2002).

[34] A. Jha, P. Chantelot, C. Clanet, and D. Quéré, *Viscous bouncing*, Soft Matter **16**, 7270 (2020).

[35] V. Sanjay, D. Lohse, and M. Jalaal, *Bursting bubble in a viscoplastic medium*, J. Fluid Mech. **922**, A2 (2021).

[36] S. Afkhami and L. Kondic, *Numerical simulation of ejected molten metal nanoparticles liquified by laser irradiation: Interplay of geometry and dewetting*, Phys. Rev. Lett. **111**, 034501 (2013).

[37] H. Wagner, *Über Stoß- und Gleitvorgänge an der Oberfläche von Flüssigkeiten*, Z. Angew. Math. Mech. **12**, 193 (1932).

[38] S. Mandre, M. Mani, and M. P. Brenner, *Precursors to splashing of liquid droplets on a solid surface*, Phys. Rev. Lett. **102**, 134502 (2009).

[39] H. Hertz, *On the contact of elastic solids*, J. Reine Angew, Math. **92**, 156 (1881).

[40] K. Langley, E. Q. Li, and S. T. Thoroddsen, *Impact of ultra-viscous drops: air-film gliding and extreme wetting*, J. Fluid Mech. **813**, 647 (2017).

[41] J. Bilotto, J. M. Kolinski, B. Lecampion, J. Molinari, G. Subhash, and J. Garcia-Suarez, *Fluid-mediated impact of soft solids*, arXiv preprint (2023).

[42] V. Bertin, *Similarity solutions in elastohydrodynamic bouncing*, J. Fluid Mech. **986**, A13 (2024).

[43] J. Philippi, P.-Y. Lagrée, and A. Antkowiak, *Drop impact on a solid surface: short-time self-similarity*, J. Fluid Mech. **795**, 96 (2016).

[44] S. Grossmann and D. Lohse, *Prandtl and Rayleigh number dependence of the Reynolds number in turbulent thermal convection*, Phys. Rev. E **66**, 016305 (2002).

[45] Y. Renardy, S. Popinet, L. Duchemin, M. Renardy, S. Zaleski, C. Josserand, M. A. Drumright-Clarke, D. Richard, C. Clanet, and D. Quéré, *Pyramidal and toroidal water drops after impact on a solid surface*, J. Fluid Mech. **484**, 69 (2003).

[46] A.-L. Biance, F. Chevy, C. Clanet, G. Lagubeau, and D. Quéré, *On the elasticity of an inertial liquid shock*, J. Fluid Mech. **554**, 47 (2006).

[47] L. Prandtl, in *Verhandlungen des III. Int. Math. Kongr., Heidelberg, 1904* (Teubner, Leipzig, 1905), pp. 484–491.

[48] H. Blasius, *Grenzschichten in Flüssigkeiten mit kleiner Reibung*, Z. Math. Phys. **56**, 1 (1908).

[49] H. Schlichting, *Boundary layer theory* (McGraw-Hill, New York, 1979).

[50] L. Prandtl, *Über Flüssigkeitsbewegung bei sehr kleiner Reibung*, Math-Kongr, Heidelberg 484 (1904).

[51] L. Onsager, *Statistical hydrodynamics*, Il Nuovo Cimento **6**, 279 (1949).

[52] B. Dubrulle, *Beyond Kolmogorov cascades*, J. Fluid Mech. **867**, P1 (2019).

[53] J. Eggers, *Role of singularities in hydrodynamics*, Phys. Rev. Fluids **3**, 110503 (2018).

[54] V. Sanjay, U. Sen, P. Kant, and D. Lohse, *Taylor-Culick retractions and the influence of the surroundings*, J. Fluid Mech. **948**, A14 (2022).

[55] J. Talukdar, U. Sen, C. Diddens, D. Lohse, and V. Sanjay, *Sliding drops on dry & wet substrates*, Working paper (2024).

[56] L. Kayal, V. Sanjay, N. Yewale, A. Kumar, and R. Dasgupta, *Focusing of concentric free-surface waves*, arXiv preprint (2024).